Soft Matter

Accepted Manuscript

This is an *Accepted Manuscript*, which has been through the Royal Society of Chemistry peer review process and has been accepted for publication.

Accepted Manuscripts are published online shortly after acceptance, before technical editing, formatting and proof reading. Using this free service, authors can make their results available to the community, in citable form, before we publish the edited article. We will replace this *Accepted Manuscript* with the edited and formatted *Advance Article* as soon as it is available.

You can find more information about *Accepted Manuscripts* in the Information for Authors.

Please note that technical editing may introduce minor changes to the text and/or graphics, which may alter content. The journal's standard Terms & Conditions and the Ethical guidelines still apply. In no event shall the Royal Society of Chemistry be held responsible for any errors or omissions in this *Accepted Manuscript* or any consequences arising from the use of any information it contains.

ROYAL SOCIETY OF CHEMISTRY

www.rsc.org/softmatter

ARTICLE TYPE

Helical inner-wall texture prevents jamming in granular pipe flows

Felix Verbücheln, Eric J. R. Parteli, and Thorsten Pöschel*

Received Xth XXXXXXXXXX 20XX, Accepted Xth XXXXXXXXX 20XX
First published on the web Xth XXXXXXXXXX 200X
DOI: 10.1039/b000000x

Granular pipe flows are characterized by intermittent behavior and large, potentially destructive solid fraction variations in the transport direction. By means of particle-based numerical simulations of gravity-driven flows in vertical pipes, we show that it is possible to obtain steady material transport by adding a helical texture to the pipe's inner-wall. The helical texture leads to more homogeneous mass flux along the pipe, prevents the emergence of large density waves and substantially reduces the probability of plug formation thus avoiding jamming of the particulate flow. We show that the granular mass flux Q through a pipe diameter D with an helical texture of wavelength λ follows the equation $Q = Q_0 \cdot \{1 - B\sin[\arctan(2\pi D/\lambda)]\}$, where Q_0 is the flow without helix, predicted from the well-known Beverloo equation. Our new expression yields, thus, a modification of the Beverloo equation with only one additional fit parameter, B, and describes the particle mass flux with the helical texture with excellent quantitative agreement with simulation results. The future application of the method proposed here has the potential to improve granular pipe flows in a broad range of processes without the need of energy input from any external source.

1 Introduction

The transport of a granular material in flow through a pipe is a process of relevance for a broad range of scientific and technological areas[1,2]. One fundamental problem in such transport is that the material flow is intrinsically unstable and characterized by large variations in solid fraction (density waves) along the pipe[3,4]. These waves induce potentially destructive pressure transients on the pipe's inner-wall and provide the mechanism responsible for the intermittent behavior of the flow.

Although the dynamics of density waves in granular pipe flows have been studied extensively in the past both experimentally[5–10] and through different types of models[3,4,11–19], it is still a challenging problem to control the mass flux of the granular material flowing through a pipe. For example, Zuriguel *et al.*[20] showed how insertion of an obstacle just above the outlet of a silo can significantly reduce the probability that the granular flow is arrested due to the formation of an arch blocking the silo's outlet[20]. However, most of the proposed strategies to control the transport along the pipe involve energy input from an external source, e.g. through application of electric fields[21] or mechanical perturbations[1,22].

Here we demonstrate a method to homogeneize the mass flux and avoid flow blockage in granular pipe flows without necessity of applying any external source of energy to the system. Our method consists of adding to the inner-wall of the pipe a helical texture, which leads to a more homogeneous distribution of the particles within the pipe thus avoiding the formation of stable plugs. By means of particle-based numerical experiments, we will show that it is possible to achieve flows with prescribed characteristics regarding the particle distribution within the pipe and the mass flow rate of the granular material by adjusting the geometric properties of the helix-shaped texture.

Felix Verbücheln, Eric J. R. Parteli and Thorsten Pöschel
Institute for Multiscale Simulation, Friedrich-Alexander University of Erlangen-Nuremberg, Nägelsbachstraße 49b, 91052 Erlangen, Germany.
** Corresponding author (T.P.): Tel: 49 9131 85 20867; E-mail: thorsten.poeschel@fau.de*

2 Numerical experiments

We simulate the process using the Discrete Element Method (DEM), that is, simultaneously solving Newton's equations of translational and rotational motion for all particles. There is a variety of models to describe the contact forces in DEM simulations, which are suitable for different particle geometry and material behavior[23–26]. In the present paper, we assume viscoelastic interaction in normal direction[27] and apply a modified Cundall-Strack model[28] for the tangential direction[29]. The corresponding forces read

$$\vec{F}_n = \min\left(0, -\rho\xi^{3/2} - \frac{3}{2}A_n\rho\sqrt{\xi}\dot{\xi}\right)\vec{e}_n\,, \qquad (1)$$

where

$$\xi = R_1 + R_2 - |\vec{r}_1 - \vec{r}_2| \qquad (2)$$

is the compression of particles of radii R_1 and R_2 at positions $\vec{r}_1$ and $\vec{r}_2$, and $\vec{e}_n \equiv (\vec{r}_1 - \vec{r}_2)/|\vec{r}_1 - \vec{r}_2|$ is the normal unit vector. The elastic parameter of Eq. (1), ρ, is a function of the Young's modulus, Y, the Poisson's ratio ν, and the effective

radius $R_{\text{eff}} \equiv R_1 R_2/(R_1+R_2)$,

$$\rho \equiv \frac{2Y}{3(1-\nu^2)}\sqrt{R_{\text{eff}}}, \quad (3)$$

while the dissipative parameter, A_n further depends on the material viscosities[27]. While ρ can be computed directly from material properties which are easily available for a variety of materials, the viscosities needed for A_n are not directly available. To determine A_n, therefore, we use a relation between the coefficient of restitution, ε, for the collision of two isolated particles, the pre-collisional velocity of these particles, v_{imp}, and A_n[30–32], where the Padé approximation is employed as described elsewhere[33].

The tangential force reads[29]

$$\vec{F}_t = -\min\left[\mu\left|\vec{F}_n\right|, \int_{\text{path}} \frac{4G}{2-\nu}\sqrt{R_{\text{eff}}\xi}\,\mathrm{d}s + A_t\sqrt{R_{\text{eff}}\xi}v_{\text{t}}\right]\vec{e}_t, \quad (4)$$

where μ is the Coulomb friction coefficient and G is the shear modulus, which is given by the equation, $2G = Y/(1+\nu)$. The integral in Eq. (4) is performed over the displacement of the particles at the point of contact for the duration of the contact[28]. Moreover, $\vec{v}_t = v_t\vec{e}_t$ stands for the relative tangential velocity at the point of contact, where $\vec{e}_t$ is the corresponding unit vector. The tangential dissipative parameter, A_t, characterizes the surface roughness and is chosen such that the prefactors of the normal and tangential deformation rates ($\dot{\xi}$ and v_{t}) in Eqs. (1) and (4), respectively, are of the same order of magnitude[34]. Using this assumption, previous authors[35] found excellent agreement between simulation results and experimental values of particle velocity profiles in a gravity-driven shearing experiment. By comparing Eqs. (1) and (4), we obtain $A_t \approx A_n Y/(1-\nu^2)$.

The integration was performed using LIGGGHTS[29], while the values of the model parameters are listed in Tab. 1. The equations used for computing the forces between particles and the internal (frictional) wall of the cylinder are the same used for modeling particle-particle collisions where one of the contact partners is of infinite mass and radius. Moreover, in order to compute the viscoelastic constant A_n using an analytical model[33], we assume a coefficient of restitution $\varepsilon \approx 0.5$ associated with a pre-collisional velocity $v_{\text{imp}} \approx 1.0\,\text{m/s}$, which is of the same order of the average axial particle velocities found in our simulations as discussed below. Using these parameters and the material properties specified in Tab. 1, we obtain $A_n \approx 7.3\times10^{-6}$ and $A_t \approx 775.9$ for particle-particle collisions, while for particle-wall collisions these values are $A_n \approx 8.4\times10^{-6}$ and $A_t \approx 891.3$.

The integration time step Δt must be small enough to accurately solve Newton's equations for the particle interaction. For undamped collisions, the duration T_{col} of the collision can be estimated using the equation[23],

$$T_{\text{col}} \approx 3.21\,(M_{\text{eff}}/\rho)^{2/5}\cdot v_{\text{imp}}^{-1/5}, \quad (5)$$

where $M_{\text{eff}} = m_1 m_2/(m_1+m_2)$ with m_1 and m_2 standing for the masses of the interacting particles. Typically a timestep smaller than about $T_{\text{col}}/50$ is recommended[36]. Since the collision time T_{col} computed using Eq. (5) with the material properties specified above is about $50\,\mu$s, we use here $\Delta t \approx 6\times10^{-7}$ s, which is below the recommended upper bound for Δt mentioned above.

Table 1 Numerical values of the parameters used in the simulations.

parameter	symbol	value
particle material density	ρ_{p}	$2650\,\text{kg/m}^3$
particle diameter	d	1.2 mm
Young's modulus	Y	10^8 Pa
Poisson's ratio	ν	0.24
Coulomb's friction coefficient	μ	0.5
pipe length	L	1 m
timestep	Δt	6×10^{-7} s

The pipe has a circular cross-section of diameter D mm and its length is $L = 1\,\text{m}$. At time $t = 0$, N particles are placed at random positions within the pipe, where N is chosen such that the sum of the volumes of all particles amounts to a prescribed fraction V_ϕ of the pipe volume. The initial velocity of the particles in radial direction is chosen randomly between $-v_r$ and v_r, with $v_r = 0.01$ m/s, while the particles have vanishing initial velocity in the axial direction ($v_z = 0$). Periodic boundary conditions are applied in the vertical (z) direction. We have performed simulations with pipes longer than $L = 1\,\text{m}$ and found that the results presented in the next Section with this value of L are not affected by finite size effects. That is, increasing the length of the pipe does not change the results.

3 Results and Discussion

We perform simulations using a constant particle diameter d as specified in Table 1 and different values of pipe diameter D. We find that the flow behavior depends fundamentally on the pipe to particle diameter ratio $D_\phi \equiv D/d$. For $D_\phi > 3$ the flow is intermittent and characterized by a *clogging* regime where the average particle velocity in the vertical direction is nearly constant (Section 3.1). For $D_\phi \lesssim 3$ *jamming* occurs thus leading to blockage of the granular flow (Section 3.2). Following the discussion of these distinct flow regimes we show in Section 3.3 that adding a helical inner-wall texture leads to a more homogeneous solid fraction distribution along the pipe thus reducing the occurrence of clogging and preventing the flow to jam.

3.1 Clogging regime

Fig. 1a shows the evolution of the total kinetic energy of particles flowing through a vertical pipe with $D_\phi = 4$. Since the initial particle velocities in the radial direction are small, the particles fall freely under the action of gravity during an initial time before colliding with the inner wall of the pipe. Collisions between the particles and between the particles and the wall lead, then, to deceleration of the particles and a decrease in the kinetic energy of the system. After a transient time, the energy gain of the particles due to gravity is nearly compensated by the energy dissipation due to collisions such that the total kinetic energy fluctuates around a constant value. The spatio-temporal image of the volume fraction along the tube (Fig. 1b) shows the emergence of density waves[3], with the development of recurrent *clogging* characterized by the formation of *plugs*, that is regions with high packing fraction (thick dark lines in Fig. 1b) which can either converge or diverge with time. The flow is inhomogeneous and associated with strong fluctuations of particle average velocities and solid fraction both in time and position along the pipe.

Fig. 1c shows the spatio-temporal image of the area-integrated particle mass flux per unit time along the tube. This flux is defined as,

$$\dot{m}(t,z) = \rho_p \varphi(t,z)\,[v_z(t,z)]\,\pi D^2/4, \qquad (6)$$

where $\varphi(t,z)$ and $v_z(t,z)$ are the packing fraction and the average particle velocity in the vertical direction, respectively, at time t within the volume element $[z+dz]\pi D^2/4$. The probability density distribution $f(\dot{m}_0)$ of the mass flux $\dot{m}_0 \equiv \dot{m}(t,0)$ at the bottom of the pipe, that is at $z = 0$, is shown in Fig. 1d. We see that $f(\dot{m}_0)$ can be well described by a lognormal distribution (fit represented by the dashed line in Fig. 1d). The expectation value of this distribution is around $0.0092\,\mathrm{kg/s}$ and nearly equals, thus, the value of mass flux associated with plug flow, denoted by the thick bright meandering lines in Fig. 1c.

Moreover, the thinner lines in the spatio-temporal plot of Fig. 1c denote faster moving particle groups and are associated with different solid fractions, as can be seen from Fig. 1b. Indeed, these lines denote smaller particles groups which occur in-between the plugs during the intermittent flow. Since these thinner lines align nearly paralell to each other, we conclude that the small interplugs particle groups move all with nearly the same average axial velocity down the pipe, independently of the value of solid fraction. Among these smaller groups, the ones with the lowest (highest) values of packing fraction are associated with the smallest (largest) values of mass flux — that is to the thin green (red) lines — in the spatio-temporal diagram of Fig. 1c. In other words, the left (right) tail of the probability density distribution in Fig. 1d incorporates the flux due to the small inter-plugs particle groups with the lowest (highest) solid fractions, whereas it is the flux due to plug flow

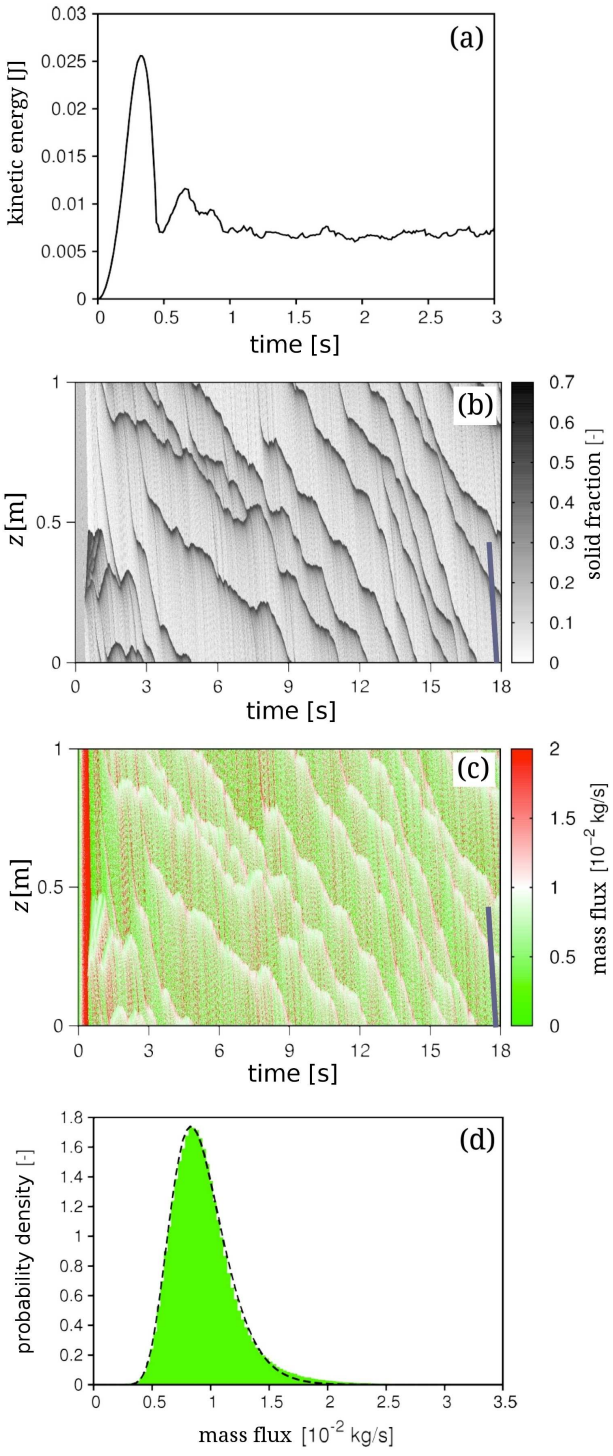

Fig. 1 Granular flow through a pipe with $D_\phi = 4$ (clogging regime). (a) Total kinetic energy of the particles as a function of time; (b) and (c) spatio-temporal images of the packing fraction and mass flux, respectively, along the tube; (d) density distribution of the time-averaged mass flow. The slope of the line at the lower right corner indicates the average axial velocity of the particles.

that dictates the expectation value of this distribution.

We have calculated $f(\dot{m}_0)$ for different values of D_ϕ within the range between 3.5 and 7.0. Fig. 2a shows the respective distributions. We see that both the distribution width and expectation value increase with the diameter ratio D_ϕ. Indeed, for given particle size and volume fraction, both the particle number and average axial velocity — and thus also the average mass flux — increase with D_ϕ. Also the distance between plugs increases with the diameter ratio D_ϕ, which means that the small inter-plugs particle groups can accelerate the longer the larger the pipe diameter.

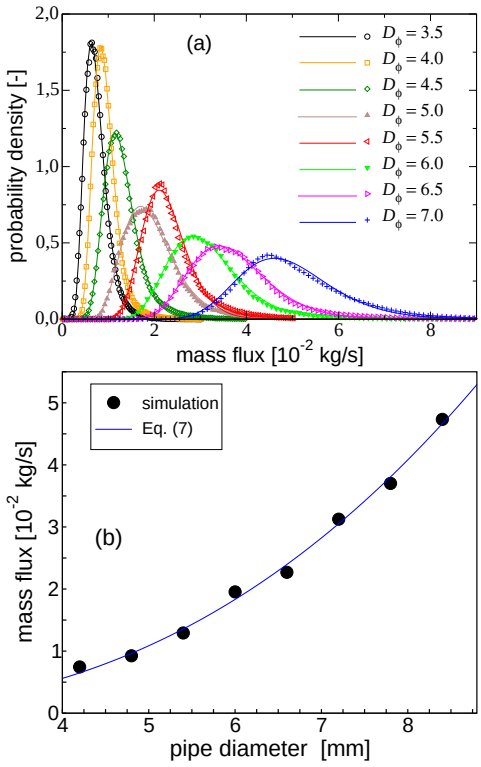

Fig. 2 Dependence of the mass flux on the pipe to particle diameter ratio D_ϕ. The particle diameter is $d = 1.2$ mm. (a) Probability density distribution of the mass flux for different values of D_ϕ. Symbols denote simulation results, lines denote fits to the data using lognormal distributions; (b) expectation value of the mass flux as a function of the pipe diameter D. Circles denote simulation results, the solid line corresponds to the best fit to these data using Eq. (7), which gives $A \approx 1.09$ and $k \approx 0.59$, with correlation coefficient $R^2 \approx 0.998$.

Moreover, in Fig. 2b we see the time-averaged flux, that is the expectation value $Q_0 = \langle \dot{m}_0 \rangle$ as a function of the pipe diameter D as obtained from the simulations (circles). Note that this mean flux can be written as $Q_0 = jA$, where $A = \pi D^2/4$ is the area of the pipe cross-section and $j = \langle v_z \rangle \rho_p V_\phi$ is the average flux density, with $\langle v_z \rangle$ denoting the average axial particle velocity. A scaling between $\langle v_z \rangle$ and the pipe diameter D can be obtained by noting that the average flow rate is dictated by the behavior of grains within the plug zones[37]. Each plug zone is associated with the formation of an unstable arch, the height of which should scale with D. Particles falling after the break of an arch can accelerate freely due to the action of gravity thus leading to a scaling of $\langle v_z \rangle$ with $\sqrt{D}$[37]. Therefore, a scaling of Q_0 with $D^{5/2}$ is expected. This scaling indeed governs the mass flux of a granular material flowing out a silo through an orifice of diameter D, which follows the well-known Beverloo equation[20,37–42],

$$Q_0 = A\rho_p \sqrt{g} \cdot (D - kd)^{2.5}, \qquad (7)$$

where the coefficients A and k must be determined from the fit to the data. Such a scaling captures well the dependence of the mass flux on the pipe diameter observed in our simulations — the best fit to the simulation data is denoted by the continuous line in Fig. 2b.

It is important to remark that, in the regime of small pipe to particle diameter ratios D_ϕ investigated here, the distribution of the flow along the pipe may be strongly affected by geometric effects as the number of possible arrangements of the particles along the cross section of the pipe affects the probability of the formation of a stable arch (see Section 3.2). Such geometrical effects may influence the width of the probability density distribution curves in Fig. 2a as the value of D_ϕ is changed — for instance, we see that for $D_\phi = 5.5$ the distribution is narrower than for $D_\phi = 6.0$ and 5.0. However, we find that the mass flux increases monotonically with D_ϕ as it can be seen in Fig. 2b.

3.2 Jamming regime

The flow characteristics described above, with constant average particle velocity and the formation of density waves along the pipe, persist over the entire simulation time, which was larger than 1000s (real time of the physical system), for all values of $D_\phi > 3$. In consistence with previous studies[43,44], we find that, for $D_\phi \lesssim 3$, *jamming* occurs thus leading to complete blockage of the granular flow. As an example of the flow in the jamming regime, we show in Fig. 3a the spatio-temporal diagram of the packing fraction for $D_\phi = 2.5$. As we can see in this figure, after about 1.8s, a large, stable plug is formed, which corresponds to the dark horizontal lines in the spatio-temporal diagram. Indeed, this plug does not break up with the impacts of the smaller particle groups that fall onto it. In order words, the frictional forces that yield the archs leading to plug formation[3] are strong enough to sustain the downward pressure on the granular column.

Our simulations show that, although the critical $D_\phi \approx 3.0$ below which complete blockage occurs is robust with respect

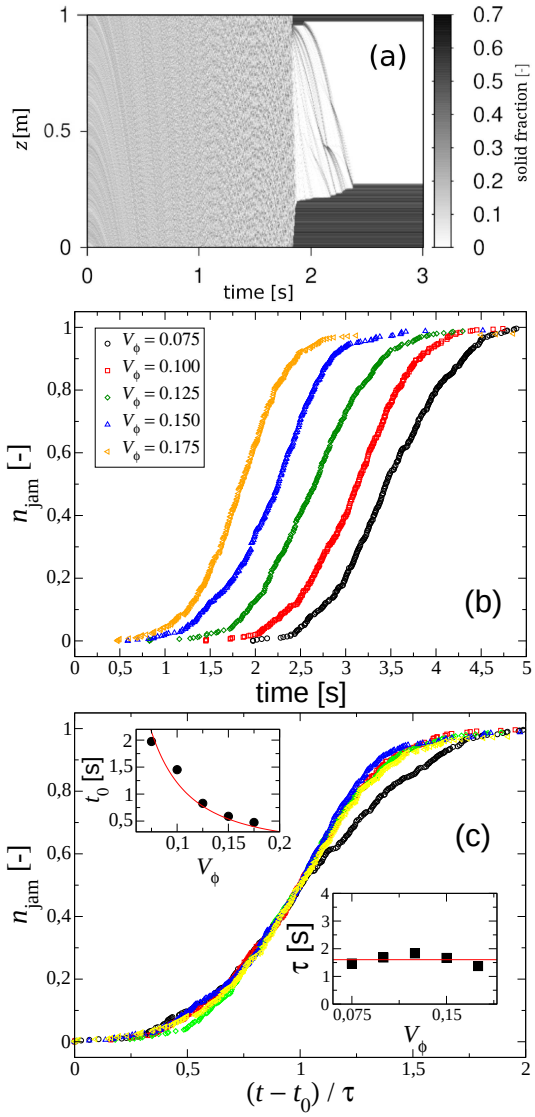

Fig. 3 (a) Cumulative distribution of the number $n_{\rm jam}$ of jammed simulations with $D_\phi = 2.5$ (jamming regime) as a function of time for different values of V_ϕ; (b) $n_{\rm jam}$ as a function of the rescaled time $(t-t_0)/\tau$, where t_0 and τ are the times at which $n_{\rm jam}$ is equal to 0.1% and 50%, respectively. The continuous lines in the upper and lower insets denote fits to the simulation data using $t_0 = a_0 V_\phi^{-2}$ and $\tau = a_\tau$, which give $a_0 \approx 0.012$ s, with correlation coefficient $R^2 \approx 0.98$, and $a_\tau \approx 1.6$ s.

to the filling volume of the particles relative to the pipe volume, V_ϕ, the time needed for the blockage to occur depends on this parameter. To quantify this dependence, we perform 100 numerical experiments for each value of V_ϕ using $D_\phi = 2.5$ which is within the jamming regime. Fig. 3b shows the resulting normalized cumulative distribution of the number of jammed simulations, $n_{\rm jam}$ as a function of time.

We see that $n_{\rm jam}$ is shifted to the left as V_ϕ increases, which means that, statistically, the flow jams the earlier the larger V_ϕ. In order to collapse all curves, we first calculate the time t_0 at which $n_{\rm jam}$ becomes larger than 0.1%. This time is shown as a function of V_ϕ in the upper inset of Fig. 3b (circles). A fit to the data using $t_0 = a_0 V_\phi^{-2}$, denoted by the continuous line, gives $a_0 \approx 0.012$ s. The main plot of Fig. 3c shows $n_{\rm jam}$ as a function of $(t-t_0)/\tau$, where τ is the time required for 50% of the simulations with a given V_ϕ to jam. As we can see in the lower inset of Fig. 3c, this characteristic time ($\tau \approx 1.6$ s) is nearly independent of V_ϕ.

These results can be understood by noting that the jamming probability increases with the probability that a stable arch along the cross section of the pipe is formed (and thus with V_ϕ). This probability further depends on D_ϕ, which controls the number of possible configurations of particles arrangements along the pipe's cross-section. For a constant $V_\phi = 0.175$, we compute $n_{\rm jam}$ for different values of $D_\phi = 2.5$, 2.6, 2.7, 2.8, 2.9 and 3.0 (see Fig. 4a). We see that for D_ϕ

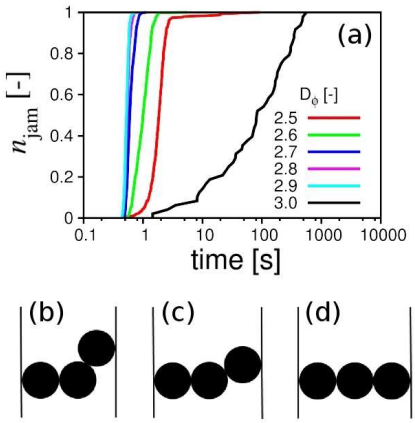

Fig. 4 (a) Cumulative distribution $n_{\rm jam}$ as a function of time for different values of D_ϕ and for constant $V_\phi = 0.175$. Note that the time is in the *logarithmic* scale; (b)−(d) show two-dimensional arrangements of particles along the cross section of the pipe with diameter ratios $D_\phi = 2.5$, 2.9 and 3.0, respectively.

within the range $2.5 \leq D_\phi \leq 2.9$ the flow jams earlier the smaller D_ϕ, whereas this trend of $n_{\rm jam}$ with D_ϕ is not obeyed by the curve corresponding to $D_\phi = 3.0$. The latter curve shows the largest jamming times among all D_ϕ in Fig. 4. To understand these results we consider the two-dimensional arrangements depicted in Figs. 4b-d. For $D_\phi = 2.9$ (Fig. 4c) the probability of stable arch formation is larger than for $D_\phi = 2.5$ (Fig. 4b), because in the former there is a higher probability to obtain a particle chain with a larger inter-particle contact area and thus a larger tangential force counter-balancing the

particle weight. However, a linear arrangement of the particles paralell to the cross-section of the pipe can be reached for $D_\phi = 3.0$ (Fig. 4d), which dramatically decreases the probability of stable arch formation. Of course a much larger number of configurations is possible considering $D_\phi > 3.0$ and three dimensional arrangements. However, although we indeed did not observe complete flow blockage for $D_\phi > 3.0$, the flow in this regime is intermittent and characterized by density waves and intermittent transport as discussed in Section 3.1 and demonstrated previously[3,4].

Therefore, in the following our aim is to develop a method to homogeneize the flow thus avoiding the formation of density waves that lead to jamming in granular pipe flows.

3.3 Flow homogeneization by means of helical inner-wall texture

Experiments aiming at reducing erosion damage from slurries in pipeline bends[45] showed that pipes which encourage swirl can get particles into suspension at lower pumping power and pressure drop than a round duct. Inspired by this observation, we investigate the vertical flow of a granular material down a pipe of circular cross-section that has a helical inner-wall texture as depicted in Fig. 5a. This texture is constituted of small beads of diameter $d_s = D/10$, which are fixed to the inner-wall of the pipe and have the material properties listed in Table 1. Each constituent bead is fixed to the wall at its center such that half hemisphere of each bead is within the inner volume of the pipe. The diameter of the pipe in the presence of the helix is adjusted such that the total volume within the pipe is the same as in the simulations without the texture elements.

Fig. 5b shows the spatio-temporal diagram of the packing fraction for the flow within a pipe with $D_\phi = 2.5$ and using the same parameters as in the simulation of Fig. 3a. As we can see jamming does not occur in such a pipe in the presence of the helical texture. A steady downward flow of the granular material is observed, whereas the particles are more homogeneously distributed throughout the pipe compared to the simulations without the helical texture. Such improvement is observed without regard of the average radial velocity of the particles. Indeed, in Figs. 6a and 6b we show the spatio-temporal diagrams of the packing fraction without and with helix texture, respectively, for the same pipe diameter but for an order of magnitude larger initial radial velocity. We see that the thick dark lines in the diagram of Fig. 6a are absent from the simulation with the helix texture (Fig. 6b). The flow in presence of the helix takes place through smaller particle groups rather than through large plugs as in the conventional duct. This result can be understood by noting that, as the particles collide with the beads fixed on the inner-wall, they are deflected to the center of the pipe, thus hindering the formation of archs. Moreover, collisions between particles and the beads

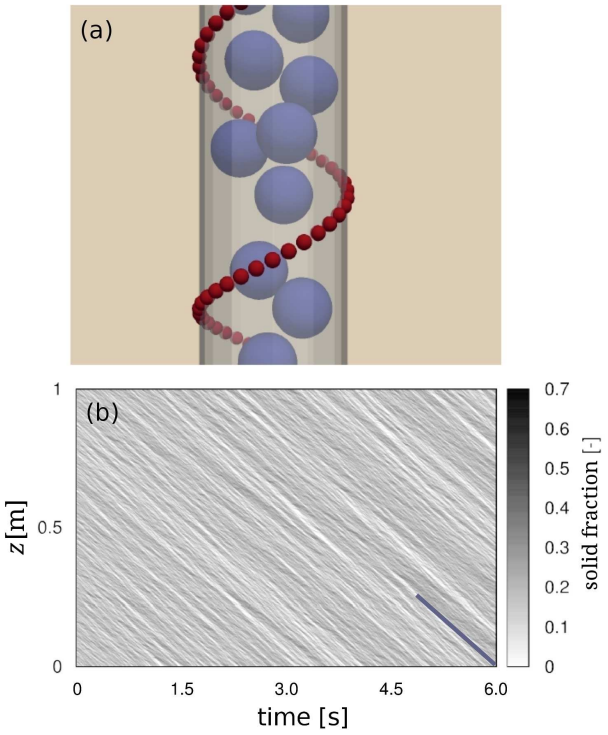

Fig. 5 (a) Flow of granular particles (blue) through a vertical pipe with $D_\phi = 2.5$ to which the helical inner-wall texture (constituted by the red beads) is applied. Initial maximal radial velocity is $v_r^{\max} = 0.01\,\mathrm{m/s}$ as in Fig. 3; (b) corresponding spatio-temporal diagram of the solid fraction along the axial position. The slope of the line at the lower right corner indicates the average axial velocity of the particles.

of the helix reduce the average axial velocity of the particles, whereas an increase in the mean radial velocity is observed (cf. Figs. 6c, 6d). Therefore, by introducing the helical textur of Fig. 5a, jamming can be prevented at the cost of a lower rate of particle flux down the pipe.

We find that the average mass flux depends significantly on the wavelength of the helix, λ. To illustrate this dependence, we show in Fig. 7 the spatio-temporal plots of the solid fraction for different values of λ obtained in a simulation wit $D_\phi = 3.5$ (which corresponds to the clogging regime describe in Section 3.1). We see that the thick lines associated with the plugs in Fig. 7a give place to an increasingly more homogeneous flow as λ decreases (cf. Figs. 7b-d). From the slope the lines in the different spatio-temporal diagrams, we also see that the average particle axial velocity increases with λ. This result can be further seen from Fig. 8, which shows the probability density functions $f(\dot{m}_0)$ of the mass flux $\dot{m}_0$ (cf. Section 3.1), for different values of λ. As λ decreases, $f(\dot{m}_0)$ approaches a Gaussian shape, that is, it becomes more sym-

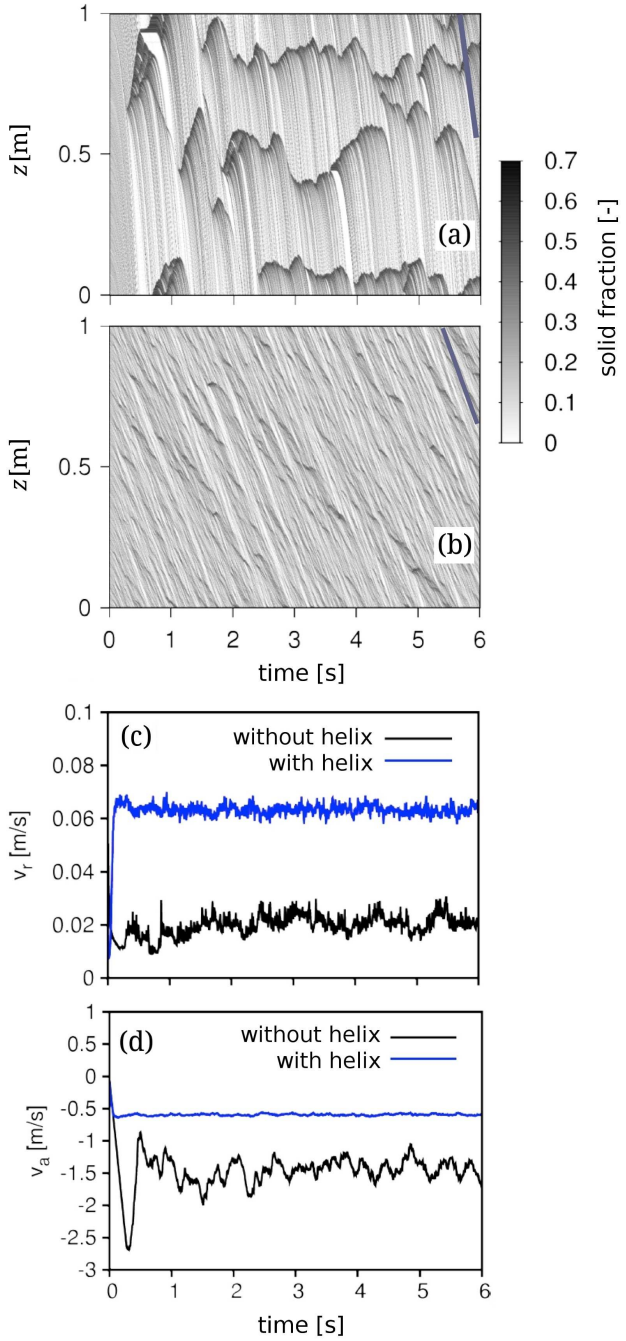

Fig. 6 Granular flow through a pipe with $D_\phi = 2.5$ and $v_r^{\max} = 0.1085\,\mathrm{m/s}$. (a) Spatio-temporal plot of the solid fraction along the pipe without helix; (b) same plot for simulation with the helix; corresponding average values of the radial (c) and axial (d) velocities along the pipe, $\langle v_r \rangle$ and $\langle v_a \rangle$, respectively. The slope of the line at the upper right corner in each plot indicates the average axial velocity of the particles.

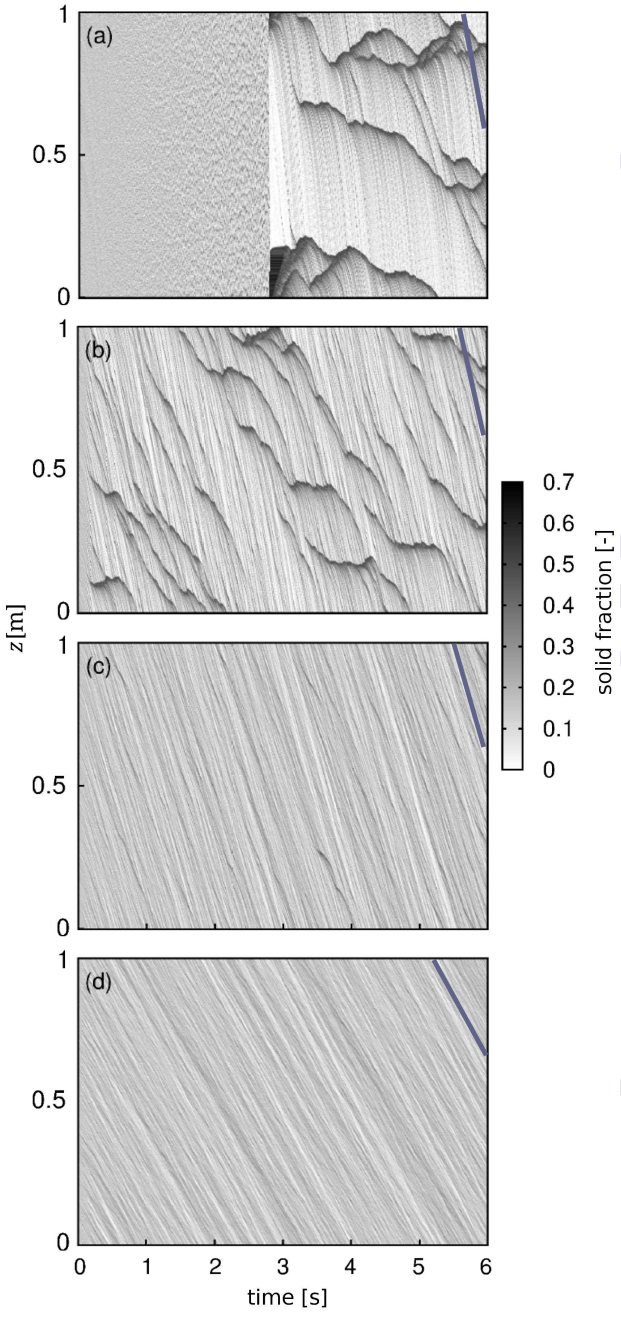

Fig. 7 (a) Spatio-temporal plots of the solid fraction along a pipe with $D_\phi = 3.5$ and without helix; the subsequent figures show the same plots for simulations with an helix of wavelength $\lambda = 1\,\mathrm{m}$ (b), 50 mm (c) and 12.5 mm (d). The slope of the line at the upper right corner in each plot indicates the average axial velocity of the particles.

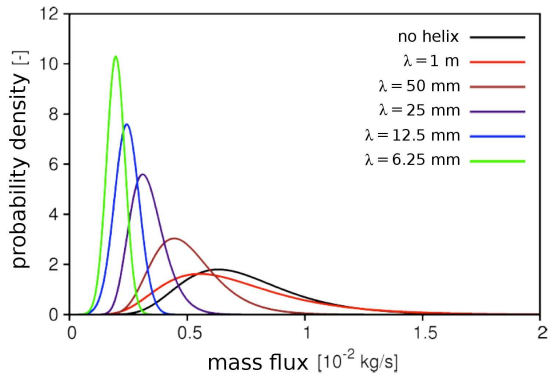

Fig. 8 Probability density distribution of the mass flux through a pipe with $D_\phi = 3.5$ (that is, pipe diameter $D = 4.2\,\text{mm}$) for different values of the helix wavelength λ.

metric, while the expectation value $Q = \langle \dot{m}_0 \rangle$ of the mass flux also decreases.

In order to quantitatively describe the effect of the helix wavelength on the mass flux, we first note that in the steady-state, the gain in momentum of the particles due to gravity is fully compensated by the momentum loss due to collisions with the pipe's inner-wall as well as with the other particles. In the presence of the helix, there is an additional contribution to the rate with which axial momentum is dissipated. This contribution, $\dot{p}_{\text{diss,helix}}$, is due to collisions of the particles with the beads composing the helix. It is reflected by a relative decrease in the magnitude of the steady-state axial velocity of the particles, compared to the value without helix, as depicted in the example of Fig. 6d. Therefore, the steady-state flux Q in the presence of the helix relates to the flux Q_0 without helix through the expression

$$Q = Q_0 - Q_{\text{diss,helix}}, \tag{8}$$

where $Q_{\text{diss,helix}}$ is the amount by which the steady-state axial mass flux is reduced when the helical texture is present.

In the small pipe to particle diameter ratio investigated here, it is reasonable to assume that the average mass flux in the axial direction is proportional to the average axial momentum of the particles, and that $Q_{\text{diss,helix}}$ is nearly proportional to $\dot{p}_{\text{diss,helix}}$. As a result of particle-helix collisions along the pipe, the particles are deflated to the pipe's central axis which is why there is an increase in the average radial momentum when the helix is present (see Fig. 6c). However, we note that due to symmetry, for any radial direction, the contribution of the collisions to increasing the radial momentum at the upper half of one helix wavelength is the same as at the lower half. For a given pipe diameter D and an helix wavelength λ made up of n_s beads, the collisions between particles with $n_s/2$ beads from the upper and lower hemispheres (halve-wavelengths) deflate the particles in *opposite* directions. We thus need to calculate the rate with each the particles gain radial momentum due to collisions with one single hemisphere. The total rate is then twice the contribution from one halve-hemisphere.

Fig. 9 represents both hemispheres unravelled from the inner-wall as two right triangles, each with legs D and $\lambda/2$. Note that $\lambda/2$ is the length corresponding to $n_s/2$ beads, which is the contribution of each hemisphere to increase the radial momentum along the pipe's cross section. Moreover, the rate of axial momentum dissipation due to each hemisphere must scale with $p_\perp$, the component of the particles' average axial momentum p_0 perpendicular to the hypothenuse of each triangle. Each of both hypothenuses in Fig. 9 encompasses $n_s/2$ beads corresponding to one helix halve-wavelength. Therefore, $\dot{p}_{\text{diss,helix}} \propto 2\,p_\perp = 2\,p_0 \sin[\Theta_{D,\lambda/2}]$, where $\Theta_{D,\lambda/2} = \arctan[\pi D/(\lambda/2)]$ (see Fig. 9). Following our assumption that $Q_{\text{diss,helix}}$

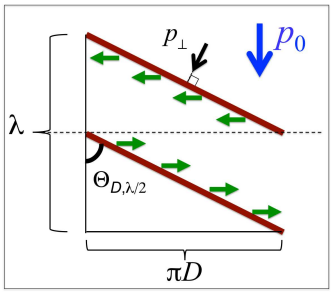

Fig. 9 Schematic diagram displaying the average axial momentum p_0 and the equivalent angle $\Theta_{D,\lambda/2} \equiv \arctan[\pi D/(\lambda/2)]$, which dictates the energy dissipation over one helix wavelength due to collisions with the $n_s/2$ beads composing one halve-wavelength of the helix. The component $p_\perp = p_0 \sin[\arctan[\pi D/(\lambda/2)]]$ is also indicated. The horizontal arrows along the helix indicate the direction from the helix to the central axis of the pipe.

should be proportional to $\dot{p}_{\text{diss,helix}}$, we can write $Q_{\text{diss,helix}} \approx 2bQ_0 \sin[\arctan[\pi D/(\lambda/2)]] = 2bQ_0 \cdot [2\pi D/\sqrt{\lambda^2 + (2\pi D)^2}]$, where b is a parameter that encodes information on the dissipative properties of the collisions. Thus, from Eq. (8),

$$\frac{Q}{Q_0} = 1 - B \cdot \left[\frac{2\pi D}{\sqrt{\lambda^2 + (2\pi D)^2}} \right], \tag{9}$$

where Q_0 is the flux without helix and the constant $B = 2b$ encodes information on energy dissipation due to collisions wit the helix. Thus, the value of B should depend on the material properties and particle diameter. To verify Eq. (9), we compute the expectation value of the flux, $Q = \int q f_\lambda(q) dq$ as a function of λ, where $f_\lambda(q)$ is the probability density functio associated with the wavelength λ as shown in Fig. 8. The result of this calculation is denoted by the symbols in the main

plot of Fig. 10b, in which Q appears rescaled with Q_0. The continuous line denotes the best fit using Eq. (9), which gives $B \approx 0.74$. As we can see from this figure, the agreement between Eq. (11) and the simulation results is excellent.

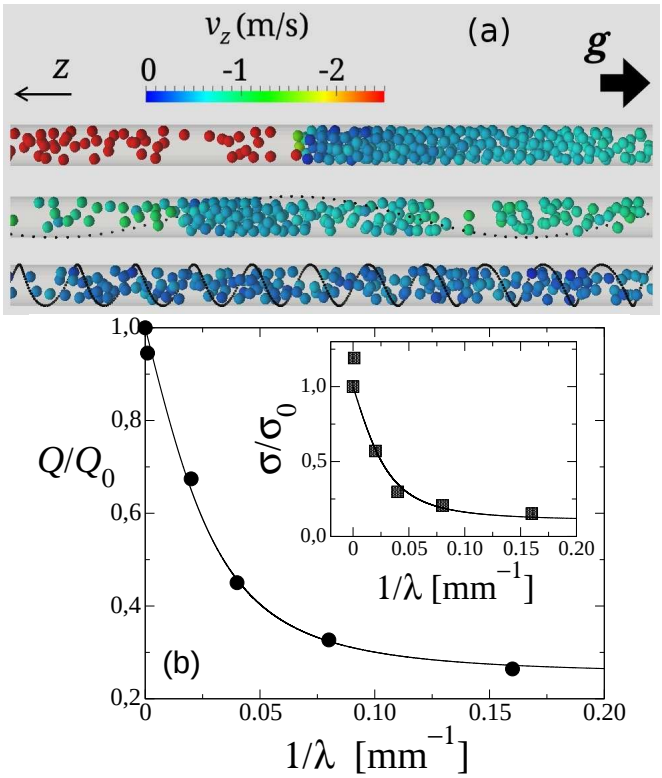

Fig. 10 (a) Snapshots of simulations without helix and with helix of wavelength values $\lambda = 25\,\text{mm}$ and 6.25 mm (from top to bottom). $D_\phi = 3.5$ and in the figures a 70 mm long excerpt of the pipe is shown. The small particles composing the helix are coloured black and there are 44 of such particles per helix wavelength; (b) main plot: expectation value of the mass flux Q as a function of $1/\lambda$, where λ is the helix wavelength and the parameters are the same as in Fig. 8. The flux is rescaled with $Q_0 \approx 7.4 \times 10^{-3}\,\text{kg/s}$ which corresponds to the calculation with no helix, or equivalently $\lambda \to \infty$. The continuous line corresponds to the best fit to the simulation data using Eq. (9), which gives $B \approx 0.75$. Inset: non-dimensional standard deviation σ/σ_0 as a function of $1/\lambda$, where $\sigma_0 \approx 2.5 \times 10^{-4}\,\text{kg/s}$ is the value of σ with no helix. The continuous line denotes the best fit to Eq. (10), which gives $C \approx 0.9$ with correlation coefficient $R^2 \approx 0.983$.

The inset of Fig. 10b shows the rescaled standard deviation of the flux, σ/σ_0, as a function of $1/\lambda$, where σ_0 is the standard deviation obtained in the simulations without helix. The value of σ/σ_0 gives a measure of the homogeneity of the flux along the pipe — the smaller σ the more homogeneous the flux. By fitting the simulation data using the equation

$$\frac{\sigma}{\sigma_0} = 1 - C \cdot \left[\frac{2\pi D}{\sqrt{\lambda^2 + (2\pi D)^2}} \right], \qquad (10)$$

we obtain $C \approx 0.9$. This fit is denoted by the continuous line in the inset of Fig. 10b. Therefore, both the flux and its standard deviation can be obtained from the geometric parameters of the helix using Eqs. (9) and (10), respectively.

Moreover, from Eq. (9) we obtain a modification of the Beverloo equation (Eq. (7)) for the flow of particulate materials in a vertical pipe of diameter D in presence of an helix of wavelength λ. By replacing Q_0 in Eq. (9) by the right-hand-side of Eq. (7), we obtain,

$$Q = A\rho_p \sqrt{g}(D - kd)^{2.5} \cdot \left\{ 1 - B \cdot \left[\frac{2\pi D}{\sqrt{\lambda^2 + (2\pi D)^2}} \right] \right\}. \qquad (11)$$

The circles in Fig. 11 show the mass flux as a function of the pipe diameter obtained for a constant helix wavelength $\lambda = 25\,\text{mm}$. The corresponding fit to the simulation data using Eq. (11) is shown by the continuous line and gives $A \approx 4.2$, $k \approx 1.13$ and $B \approx 1.05$. We see that the agreement with the data is very good. However, obviously Eq. (11) can only be valid for the regime of small pipe to particle diameter ratios investigated here. Indeed, the fit in Fig. 11 shows a maximum at $D_\phi \approx 6.5$, and predicts negative flux values for $D_\phi \gtrsim 10$. Moreover, as $\lambda \to 0$ the flux through the pipe must follow the original Beverloo equation with Q_0 corresponding to a pipe

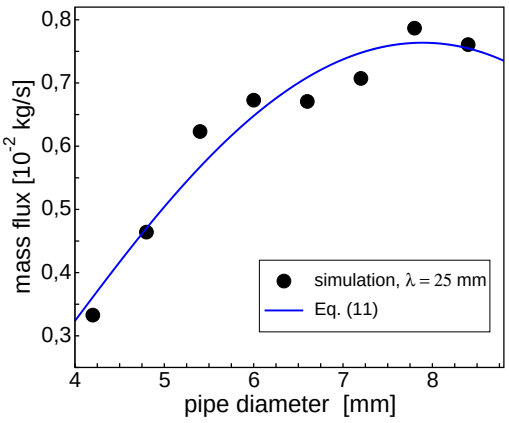

Fig. 11 Expectation value of the mass flux as a function of the pipe diameter D for simulations using an helical inner-wall texture with $\lambda = 25\,\text{mm}$. The particle size is $d = 1.2\,\text{mm}$ and the solid fraction $V_\phi = 0.15$ is the same as in Fig. 2 (which considers simulations with no helix). Circles denote simulation results, and the continuous line denotes the best fit to these data using Eq. (11), which gives $A \approx 4.2$, $k \approx 1.13$ and $B \approx 1.05$, with $R^2 \approx 0.976$.

with no helix and diameter $D - d_s$, where d_s is the size of the spheres constituting the helix. Further work is thus needed in order to elucidate the dependence of the coefficients A, B, C and k on the number of helix beads per wavelength λ, as well as on the particles' frictional and dissipation properties.

Our results raise the question whether other inner-wall texture geometries have a similar effect as the helical one. We thus perform simulations using $V_\phi = 0.15$ and $D_\phi = 2.5$ with the helix geometry as well as with three further alternative textures (Fig. 12).

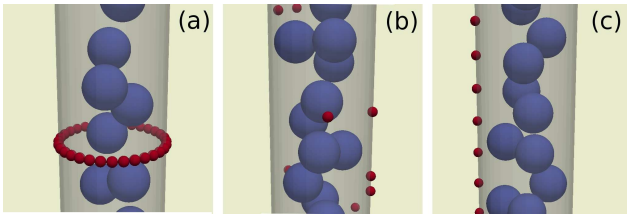

Fig. 12 Alternative texture geometries: (a) rings, (b) randomly distributed and (c) vertically aligned beads fixed on the inner-wall of the pipe. The number of particles constituting the different textures is the same as for an helical texture of wavelength $\lambda = 23\,\mathrm{mm}$.

The first of these alternative geometries consists of rings disposed perpendicularly to the transport direction along the pipe axis and with spacing equal to λ. Each ring is made of the same type of beads that form the helix, and the number of beads in a ring is equal to the number of beads in one wavelength of the helix (Fig. 12a). The spatio-temporal diagrams obtained with the helix and with the rings are shown in Figs. 13a and 13b, respectively. We see that the texture made of rings does not favour steady flow in vertical pipes as does the helical one. Directly on top of each ring there occurs accumulation of particles and the formation of dense plugs which can lead to stable archs thus eventually causing blockage of the flow.

The second alternative geometry consists of disposing the constituent beads of the texture randomly over the entire inner-wall surface of the pipe (Fig. 12b). Hereby the same total number of constituent beads as in the helical texture is applied. By comparing the corresponding spatio-temporal diagram (Fig. 13c) with the one associated with the helix (Fig. 13a), we see that the latter texture geometry yields a larger particle flux — the particle axial velocity for the helix geometry is $0.71\,\mathrm{m/s}$, while for the random texture it is $0.39\,\mathrm{m/s}$.

Finally, in the third alternative geometry the particles are arranged into a vertical line fixed on the inner-wall over the entire tube length (Fig. 12c). The spatio-temporal diagram of the simulation using such a texture, shown in Fig. 13d, displays the occurrence of dense plugs and inhomogeneous flow.

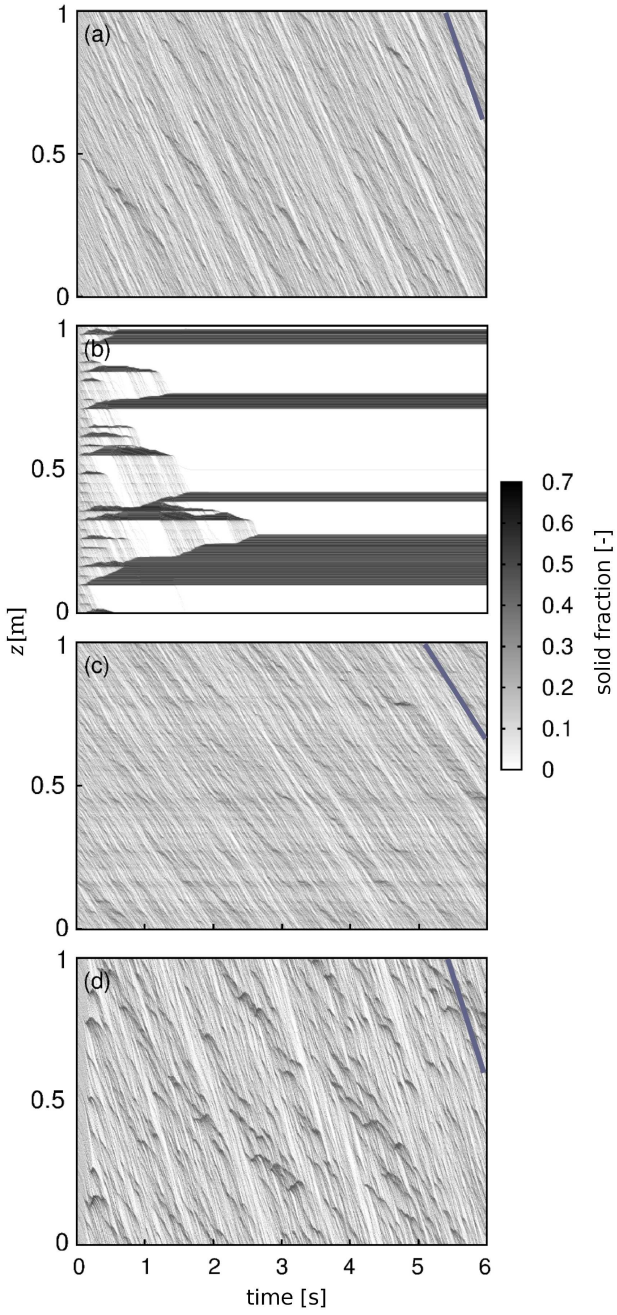

Fig. 13 Spatio-temporal plots of the solid fraction along the pipe for different types of inner-wall textures: (a) helix, (b) rings, (c) randomly distributed beads on the pipe inner-wall and (d) beads forming a single line that is paralell to the pipe axis. The slope of the line at the upper right corner in each plot indicates the average axial velocity of the particles.

Overall, the flow using the texture geometry in the form of a helix or using beads disposed randomly along the pipe is more homogeneous than the flow using the linear texture geometry.

Based on the results of our simulations, we conclude that the alternative textures are inferior to the helical inner-wall one since they lead either to inhomogeneous flow or to smaller mass flux values.

4 Conclusions

In conclusion, we have presented a method to obtain steady flows of granular materials through narrow pipes, which consists of applying a helical texture to the pipe's inner wall. In presence of such a texture, particles impingements are more homogeneouly distributed along the pipe, which substantially reduces the solid fraction fluctuations that are inherent to particulate flows through narrow channels. Our simulations show that, by tuning the wavelength of the helix, it is possible to achieve flows with prescribed transport characteristics. Specifically, we have shown that the mass flux in presence of the helix can be predicted as a function of the pipe diameter and helix wavelength using an expression that is a modification of the well-known Beverloo equation with only one additional fit parameter. Excellent quantitative agreement between the values of mass flux predicted from our expression with the mass flux values obtained from simulation results was found.

To the best of our knowledge, there is no direct experimental evidence of the effect of an helical inner-wall texture on the flow of granular materials in vertical pipes, the present results could be compared to. However, as stated before, it was already shown experimentally that erosion damage from granulates in fluid flow through pipeline bends can be diminished by using helically-formed pipes, because such pipes, which encourage *swirl*, lead to a more homogeneous particle concentration [45].

The helical inner-wall texture provides a means to homogeneize the flow along the *entire* pipe without the need of energy input from any external source. In fact, previous methods to obtain steady granular flows were either based on energy input to the system, e.g. through electric fields or mechanical perturbations [1], or designed to prevent the blockage at the end of silos by adding an obstacle near the flow outlet [20]. Our method has proven efficient to prevent the formation of density waves which are inherent to the flow of granular materials through pipes and occur without regard of the pipe to particle diameter ratio. We remark that the density waves in vertical pipe flows occur at low packing fraction values and that the necessary condition for jamming in such flows is the formation of a stable plug that does not break due to collisions of particles falling upon it thus leading to flow blockage and formation of a stable column. This mechanism is thus different from the shear-jamming mechanism where a dense granular system, which is already close to its highest packing fraction associated with the jammed stated, is driven to a shear-jammed state by application of a shear stress under constant density [46–49].

We believe that application of the helical texture presented here could be used to enhance not only gravity-driven pipe flows but also fluid-driven particle transport through both through vertical and horizontal pipes [18,50], which remains to be investigated in the future. It would be thus interesting to perform experiments on vertical or horizontal pipe flows that include an helical inner-wall texture to verify the predictions from our numerical simulations.

Acknowledgements

We thank Patric Müller, Dan Serero, Severin Strobl and Nikola Topic for discussions. We thank the German Research Foundation (DFG) for funding through the Cluster of Excellence "Engineering of Advanced Materials" and the Collaborative Research Center SFB814 (Additive Manufacturing). We gratefully acknowledge the computing time granted by the John von Neumann Institute for Computing (NIC) and provided on the supercomputer JUROPA at Jülich Supercomputing Centre (JSC).

References

1 C. Liu, P. Wu and L. Wang, *Soft Matter*, 2013, **9**, 4762–4766.
2 K. To, P. Y. Lai and H. K. Pak, *Phys. Rev. Lett.*, 2001, **86**, 71–74.
3 T. Pöschel, *J. Phys. I France*, 1994, **4**, 499–506.
4 T. Riethmüller, L. Schimansky-Geier, D. Rosenkranz and T. Pöschel, *J. Stat. Phys.*, 1997, **86**, 421–430.
5 T. Le Pennec, M. Ammi, J. C. Messager, B. Truffin, D. Bideau and J. Garnier, *Powder Technology*, 1995, **85**, 279–281.
6 O. Moriyama, N. Kuroiwa, M. Matsushita and H. Hayakawa, *Phys. Rev. Lett.*, 1998, **80**, 2833–2836.
7 J. L. Aider, N. Sommier, T. Raafat and J. P. Hulin, *Phys. Rev. E*, 1999, **59**, 778–786.
8 Y. Bertho, F. Giorgiutti-Dauphiné, T. Raafat, E. J. Hinch, H. J. Herrmann and J. P. Hulin, *J. Fluid Mech.*, 2002, **459**, 317–345.
9 Y. Bertho, F. Giorgiutti-Dauphiné and J. P. Hulin, *Phys. Fluids*, 2003, **15**, 3358–3369.
10 O. Moriyama, N. Kuroiwa, S. Tateda, T. Arai, A. Awazu, Y. Yamazaki and M. Matsushita, *Prog. Theor. Phys. Supp.*, 2003, 136–146.
11 R. Gudhe, R. C. Yalamanchili and M. Massoudi, *Int. J. Non-Linear Mechanics*, 1994, **29**, 1–12.
12 J. Lee and M. Leibig, *J. Phys. I France*, 1994, **4**, 507–514.
13 G. Peng and H. J. Herrmann, *Phys. Rev. E*, 1995, **51**, 1745–1758.
14 A. Valance and T. Le Pennec, *Eur. Phys. J. B*, 1998, **5**, 223–229.
15 E. D. Liss, S. L. Conway and B. J. Glasser, *Physics of Fluids*, 2002, **14**, 3309–3326.
16 E. D. Liss, S. L. Conway, J. A. Zega and B. J. Glasser, *Pharmaceutical Technology*, 2004, **February**, 78–96.
17 I. Bratberg, F. Radjai and A. Hansen, *Phys. Rev. E*, 2005, **71**, 011301.
18 M. Strauss, S. McNamara, H. J. Herrmann, G. Niederreiter and K. Sommer, *Powder Technolgy*, 2006, **162**, 16–26.
19 S. Å. Ellingsen, K. S. Gjerden, M. Grøva and A. Hansen, *Phys. Rev. E*, 2010, **81**, 061302.

20 I. Zuriguel, A. Janda, A. Garcimartín, C. Lozano, R. Arévalo and D. Maza, *Phys. Rev. Lett.*, 2011, **107**, 278001.
21 W. Chen, M. Hou, K. Lu, Z. Jiang and L. Lam, *Phys. Rev. E*, 2001, **64**, 061305.
22 M. L. Hunt, R. C. Weathers, A. T. Lee, C. E. Brennen and C. R. Wassgren, *Physics of Fluids*, 1999, **11**, 68–75.
23 J. Schäfer, S. Dippel and D. E. Wolf, *J. Phys. I France*, 1996, **6**, 5–20.
24 T. Pöschel and T. Schwager, *Computational Granular Dynamics*, Springer, Heidelberg, 2005.
25 H. Kruggel-Emden, E. Simsek, S. Rickelt, S. Wirtz and V. Scherer, *Powder Technol.*, 2007, **171**, 157–173.
26 H. Kruggel-Emden, S. Wirtz and V. Scherer, *Chem. Eng. Sci.*, 2008, **63**, 1523–1541.
27 N. V. Brilliantov, F. Spahn, J.-M. Hertzsch and T. Pöschel, *Phys. Rev. E*, 1996, **53**, 5382–5392.
28 P. A. Cundall and O. D. L. Strack, *Geotechnique*, 1979, **29**, 47–65.
29 C. Kloss, C. Goniva, A. Hager, S. Amberger and S. Pirker, *www.liggghts.com; Prog. Comput. Fluid Dy.*, 2012, **12**, 140–152.
30 T. Schwager and T. Pöschel, *Phys. Rev. E*, 2008, **78**, 051304.
31 T. Schwager and T. Pöschel, *Phys. Rev. E*, 1998, **57**, 650–654.
32 R. Ramírez, T. Pöschel, N. V. Brilliantov and T. Schwager, *Phys. Rev. E*, 1999, **60**, 4465–4472.
33 P. Müller and T. Pöschel, *Phys. Rev. E*, 2011, **84**, 021302.
34 T. Schwager, V. Becker and T. Pöschel, *Eur. Phys. J. E*, 2008, **27**, 107–114.
35 C. H. Rycroft, A. V. Orpe and A. Kudrolli, *Phys. Rev. E*, 2009, **80**, 031035.
36 L. E. Silbert, D. Ertaş, G. S. Grest, T. C. Halsey, D. Levine and S. J. Plimpton, *Phys. Rev. E*, 2001, **64**, 051302.
37 C. Mankoc, A. Janda, R. Arévalo, J. M. Pastor, I. Zuriguel, A. Garcimartín and D. Maza, *Granular Matter*, 2007, **9**, 407–414.
38 W. A. Beverloo, H. A. Leniger and J. van de Velde, *Chemical Engineering Science*, 1961, **15**, 260–269.
39 G. H. L. Hagen, *Poggendorfs Ann. Phys. Chem.*, 1839, **46**, 423–442.
40 R. M. Nedderman, U. Tüzün, S. B. Savage and G. T. Houlsby, *Chemical Engineering Science*, 1982, **37**, 1597–1609.
41 B. P. Tighe and M. Sperl, *Granul. Matter*, 2007, **9**, 141–144.
42 A. Janda, I. Zuriguel, J. Bienzobas, A. Garcimartín and D. Maza, *AIP Conf. Proc.*, 2013, **1542**, 710–713.
43 C. A. Shook and M. C. Roco, *Slurry Flow: Principle and Practice*, Butterworth-Heinemann, Stoneham, MA, 1991.
44 J. Hadjigeorgiou and J. F. Lessard, *International Journal of Rock Mechanics & Mining Sciences*, 2007, **44**, 820–834.
45 R. J. K. Wood, T. F. Jones, N. J. Miles and J. Ganeshalingam, *Wear*, 2001, **250**, 770–778.
46 D. Bi, J. Zhang, B. Chakraborty and R. P. Behringer, *Nature*, 2011, **480**, 355–358.
47 M. Pica Ciamarra, P. Richard, M. Schröter and B. P. Tighe, *Soft Matter*, 2012, **8**, 9731.
48 M. S. van Deen, J. Simon, Z. Zeravcic, S. Dagois-Bohy, B. P. Tighe and M. van Hecke, *Phys. Rev. E*, 2014, **90**, 020202(R).
49 R. Arévalo and M. Pica Ciamarra, *Soft Matter*, 2014, **10**, 2728.
50 E. W. C. Lim, C.-H. Wang and A. B. Yu, *AIChE Journal*, 2006, **52**, 496–509.